PERSPECTIVE | MAY 20 2025

Emerging thermal metrology for ultra-wide bandgap semiconductor devices

D. Myren ; F. Vásquez-Aza ; J. S. Lundh ; M. J. Tadjer ; G. Pavlidis

Appl. Phys. Lett. 126, 200502 (2025)
https://doi.org/10.1063/5.0256723

Applied Physics Letters PERSPECTIVE pubs.aip.org/aip/apl

Emerging thermal metrology for ultra-wide bandgap semiconductor devices

Cite as: Appl. Phys. Lett. **126**, 200502 (2025); doi: 10.1063/5.0256723
Submitted: 6 January 2025 · Accepted: 7 May 2025 ·
Published Online: 20 May 2025

D. Myren,[1] F. Vásquez-Aza,[1] J. S. Lundh,[2] M. J. Tadjer,[2] and G. Pavlidis[1,a)]

AFFILIATIONS

[1]School of Mechanical Aerospace and Manufacturing Engineering, University of Connecticut, Storrs, Connecticut 06269, USA
[2]U.S. Naval Research Laboratory, 4555 Overlook Ave. SW, Washington, DC 20375, USA

[a)]Author to whom correspondence should be addressed: georges.pavlidis@uconn.edu

ABSTRACT

Ultrawide bandgap (UWBG) semiconductor materials, such as $\beta - Ga_2O_3$ (gallium oxide), AlN (aluminum nitride), $Al_xGa_{1-x}N$ (AlGaN), and diamond, have emerged as essential candidates for components in high-power, high-frequency applications due to their superior electronic properties. However, with the exception of diamond and AlN, these materials present unique thermal management challenges, primarily because of their low thermal conductivities that are incapable of managing the demand for high power densities. Therefore, novel thermal management approaches that feature new device architectures are needed to prevent excessively high peak temperatures in UWBG devices. In parallel, accurate device-level thermal characterization (with high spatial/temporal resolution) is crucial to verify and optimize these designs with an overall goal to improve device performance and reliability. This paper discusses current thermal metrology techniques used for UWBG semiconductor devices covering: optical methods (Raman and thermoreflectance); electrical methods (gate resistance thermometry); and scanning probe methods (scanning thermal microscopy). More specifically, the steady-state and transient capability of each thermal metrology is explored and the limitation of each technique is highlighted. Finally, this perspective outlines potential advances in transient thermoreflectance imaging including a hyperspectral approach for nitride based heterostructures and a sub-bandgap excitation technique for gallium oxide based electronics. Additionally, the development of a future thermoreflectance microscope is presented. This microscope features high optical transmission, in the deep ultra violet wavelength range, for near bandgap thermoreflectance imaging of UWBG devices.

I. ULTRAWIDE BANDGAP SEMICONDUCTOR TECHNOLOGIES FOR HIGH POWER APPLICATIONS

The semiconductor industry has evolved through phases of innovation to meet the increasing demands for devices operating at higher power and frequency. Although silicon (Si) has historically dominated due to its abundance and ease of processing, increasing demands for a higher power density and switching frequency have limited the electrothermal performance of Si based components and have prompted the adoption of wide bandgap (WBG) semiconductors such as gallium nitride (GaN) and silicon carbide (SiC).[1] To achieve further advancements in the device performance, researchers are exploring the adoption of ultrawide bandgap (UWBG) semiconductors, characterized by bandgaps > 3.4 eV.[2] These materials, such as gallium oxide, AlN, AlGaN, and diamond, exhibit high breakdown electric fields, thermal stability, and low intrinsic carrier concentrations, making them promising for the next-generation power and RF transistors with high-field, high-temperature, high-frequency applications.[1–3]

A comparison of the thermal and electrical properties of relevant semiconductors for power and RF electronics is summarized in Table I. Electrically, the high critical field of UWBG semiconductors enables devices to withstand large potential differences across reduced channel spacings ($<2\,\mu$m), enabling device/system miniaturization through reduced circuit component requirements as well.[3] On the other hand, despite the improved thermal resilience associated with the wider bandgap,[1,3,4] the higher power densities will lead to localized Joule heating that generates hot spots on the order of 1 μm or less. The resulting temperature profile will feature steep temperature gradients (10–15 °C/μm),[5] which will generate significant thermal stress near interfaces (up to GPa) due to the mismatch in the coefficient of thermal expansion.[6] With thermal conductivities ranging from 10 to 30 $Wm^{-1}K^{-1}$ for most UWBG semiconductors (diamond and AlN being notable exceptions), efficient heat dissipation becomes a critical challenge to ensure the reliability and performance of devices.[3] Moreover, the poor thermal properties of UWBG semiconductors, especially oxides and ternary alloys, result in orders of magnitude

TABLE I. Key electrical and thermal parameters of selected semiconductor materials.

Material	Bandgap (eV)	Bulk critical field (MV/cm)	Carrier mobility ($cm^2V^{-1}s^{-1}$)	Thermal conductivity ($Wm^{-1}K^{-1}$)	Thermal diffusivity (cm^2s^{-1})
Si	1.12[7]	0.3[7]	Channel:[a] 1400[8]	159[7]	0.97
6H-SiC	3.02[9]	2.5[9]	Channel:[a] 1020[8]	390 in-plane[10]	1.62
4H-SiC	3.26[9]	2.2[9]	Channel:[a] 1020[8]	415 in-plane[10]	1.72
GaN	3.4[7]	3[7]	2DEG Channel:[b] 2000[8]	230[11]	0.87
$\beta - Ga_2O_3$	4.8[2]	10.3[2]	Electron: 180[1] Hole: -[1]	11-27[12]	0.07
Diamond	5.5[2]	13[2]	Electron: 4500[1] Hole:3800[1]	2290[2]	12.5
$Al_{0.85}Ga_{0.15}N$[c]	5.61[8]	10.7[8]	Channel:[a] 250[8]	8.5[8]	0.03
AlN	6[2]	12.3[13]	Electron: 426[1] Hole: -[1]	319[14]	1.36

[a]Channel carrier mobilities are combined hole and electron mobilities measured in representative devices.[8]
[b]Combined mobility in the 2DEG.[8]
[c]The properties of AlGaN vary non-linearly with the aluminum content.

lower thermal diffusivity compared to binary nitride and carbide compounds, directly impacting the device's dynamic cooling and heat accumulation.

Thermal characterization of semiconductors has traditionally been conducted using optical techniques[15,16] to understand the fundamental thermal transport across sub-micrometer thin films and interfaces present in device structures. Example studies include: impact of impurities/dislocations on thermal conductivity;[17] film/substrate thermal boundary resistance;[18] and thickness and temperature-dependent thermal conductivities.[19] However, material-level thermal characterization cannot elucidate the thermal impact of device operation, such as field distribution effects and device geometry,[20] which is unique to a functioning device. Therefore, advanced thermal metrology techniques with high spatial ($<1\,\mu m$) and temporal resolution (<200 ns) are essential to optimize heat dissipation and fully exploit the potential of UWBG semiconductor devices.[8] In contrast to single point measurements, thermal mapping will provide guidelines for device geometry and quantify the impact of biasing, thermal crosstalk, and buffer layer selection. Beyond the thermal challenges, widespread adoption of UWBG semiconductors (except gallium oxide) faces practical obstacles such as limited substrate availability with high costs, and yield processing issues.[1] The ability to dope both n-type and p-type also remains a barrier for some UWBG semiconductors.[1,2] By combining exceptional electrical properties with ongoing improvements in thermal management and manufacturing, UWBG materials represent a transformative step forward in semiconductor technologies for high-power and high-frequency applications.

II. DEVICE LEVEL THERMAL CHARACTERIZATION STRATEGIES

Accurate temperature profiles with sub-micrometer spatial resolution are crucial to understanding the thermal behavior of UWBG devices. Dimensional analysis using the Biot number ($Bi = h \cdot L/k$), Knudsen number ($Kn = \Lambda/L$), and Fourier number ($Fo = \alpha \cdot t/L^2$), with the thermal diffusivity α defined in the typical manner ($\alpha = k/\rho c_p$), will tend toward $Bi \ll 1$, $Kn \approx 1$, and $Fo \ll 1$. A low Fourier number (Fo) will result in highly localized heating, whereas a low Biot number (Bi) demonstrates that conduction is the nearly exclusive mode of heat transfer throughout the thin film structure. Moreover, a high Knudsen number (Kn) confirms that nanoscale phonon effects will be highly relevant to the conduction process.[4,21] The relevant phonon effects are boundary, defect, and Umklapp scattering. Boundary scattering, which occurs at film interfaces, may be well understood by pump-probe thin-film measurements [time and frequency domain thermoreflectance (TDTR and FDTR)][16] and can be fairly well predicted analytically.[22] Defect scattering[22] (a mechanism that governs thermal conductivity at low temperatures) can occur in natural, strain-induced, and manufacturing-induced defects (etching, metallization, doping, etc.).[22] Umklapp scattering, which results from the net momentum in phonon scattering not being conserved, causes decreases in thermal conductivity with increasing temperature and will exacerbate poor thermal transport.[12]

In addition to the phonon and thin crystal film effects, heat transfer in WBG/UWBG devices is also a function of the electrical field (bias-dependent Joule heating).[23,24] The non-uniformity of the Joule heating profile originates from the change in the electric field across the channel. Specifically, during RF operation, the voltage swing applied to the gate will change the location of the peak temperature in the device.[25,26] This time-dependent phenomenon prevents device engineers from relying on one thermal measurement technique to estimate the peak temperature for lifetime and reliability.[27] This suggests that direct thermal mapping of devices, coupled with thermal conductivity measurements of the devices' constituent materials, is essential for electro-thermal co-design of UWBG semiconductor devices.[8]

The experimental methods discussed in Table II are key methods in use for the study of semiconductor devices. This is not an exhaustive list; notable absences include time domain thermoreflectance (TDTR), frequency domain thermoreflectance (FDTR), and steady-state thermoreflectance (SSTR), which are generally more valuable from a materials characterization perspective than for the characterization of devices.[16] As suggested by the non-dimensional analysis, the experimental methods should have spatial and temporal resolution better

TABLE II. Comparison of some thermal metrology methods.

Method	Lateral resolution (μm)	Temporal resolution (ns)	Widefield capability	Surface temperature capability	Restrictions
TTI	0.265	50	Yes	Yes	Wavelength-material matching
GRT	N/A	$\approx$0.1[a]	No	No	Metallic structures
Raman Spectroscopy	0.354[b]	$\gg$1000[c]	Yes[d]	No	Nonmetallic materials[e]
SThM	0.050	$\approx$0.1[a]	No	Yes	Contact measurement
Infrared Thermal Imaging	5	$\approx$270[f]	Yes	Yes	May require coatings

[a]Technique is limited by thermal propagation into the metallic structure and the speed at which a signal may be detected electrically. At the time of writing, oscilloscopes capable of approximately 10 GHz sampling are available, corresponding to 0.1 ns resolution, but with finite heat transfer rates, the real resolution is likely somewhat longer.
[b]Limited by the wavelength of the chosen excitation laser and numerical aperture (NA) of the optical system. This resolution is calculated for a typical laser wavelength of 532 nm with a systemic NA of 0.75.
[c]Long acquisition times are typical with conventional Raman spectrometers, but modern developments in the field of high-speed and transient Raman are quite promising.[31]
[d]Considering the use of Raman active nanoparticles to ensure a surface reading. Otherwise, there are important depth averaging factors to consider.
[e]The use of Raman active nanoparticles can allow measurement of metallic structures, as the nanoparticles themselves.
[f]Based on the availability of commercial high speed IR cameras.

than approximately 1 μm and 100 ns in order to monitor the behavior of localized heating clusters during operation. For this reason, thermal characterization methods that rely solely on DC and/or pulsed electrical characterization data are of limited utility compared to the techniques discussed in this perspective because they will only resolve average temperatures within the device and may not fully capture any locally and spatially discrete regions of interest.[28] As long as signal to noise ratio is tolerable, better spatial and temporal resolution is desirable. Measurements would also ideally be non-contact to avoid interference with the thermal and electron transport processes, but it is sufficient to use methods that do not disturb these processes or do so in a well-understood manner.

All optical methods are ultimately diffraction limited and dependent on the wavelength being used for the measurement.[29] Thermoreflectance imaging (TTI) and Raman spectroscopy, which typically use visible wavelengths, permit for sub-micron spatial resolutions. Infrared (IR) thermal imaging, due to the associated long IR wavelengths, however, is limited spatially to resolutions of approximately 5 μm and thus better suited for high throughput thermal mapping on the system and package level.[30]

A. Transient thermoreflectance imaging (TTI)

TTI is a lock-in technique that leverages linear changes in reflectivity as a function of temperature to create submicrometer resolution thermal maps.[32] LED and laser-based TTI methods exist, with different advantages and challenges.[33–35] This paper focuses on the LED-based approach due to the wide-field nature of the measurement, low intensity of the light used that may minimize photo-induced currents,[35] and the ease by which LED sources may be changed on our experimental apparatus. By uniformly illuminating the device surface with a collimated monochromatic light emitting diode (LED), a charged coupled device (CCD) camera is used to measure the change in reflection of each pixel (reaching down to 55 nm/pixel with an 100 $\times$ objective).[36] The highest signal to noise ratio for TTI is achieved when synchronizing the device pulse (<30% duty cycle) and LED pulse (<2% duty cycle) to capture the reflectance change between the device's ON and OFF state. The time delay between the LED and the device pulsing can be varied to capture the structure's transient temperature rise and decay. Through the implementation of a piezoelectric stage with advanced auto-focusing features, TTI images can be averaged over thousands of cycles (with acquisition times < 1 min) to provide localized temperature variations within a device. The distribution at each time step may also be considered sequentially to evaluate the transient behavior. This technique is non-contact, allowing temperature measurements without physically altering the intrinsic device operation. Furthermore, TTI can reach temporal resolutions down to 50 ns (minimum stable pulse width of a commercial LED) to dynamically characterize power switching devices up to 5 MHz.[15,37,38] However, TTI's sensitivity depends on the optical and electrical properties of the material, as discussed in further detail in Sec. III, which has offered very significant challenges with UWBG materials.

In principle, TTI depends on the change in reflectivity that occurs on a material surface as its temperature changes. The commonly used linear approximation of the relationship is shown in Eq. (1), where at a specific wavelength the change in reflectivity and the reflectivity at a reference condition (OFF-state), ΔR and R, respectively, is related to a change in temperature (ΔT) through the thermoreflectance coefficient C_{TH},[16]

$$\frac{\Delta R}{R} = \left(\frac{1}{R}\frac{\delta R}{\delta T}\right)\Delta T = C_{TH}\Delta T. \quad (1)$$

The calibration of a TTI experiment involves setting the device at a constant uniform temperature (T_{cold}) and measuring the relative change in reflected intensity ($\Delta R/R$) using monochromatic excitation between this reference state, T_{cold}, and when the device temperature is elevated (T_{hot}). Typically, the calibration is performed with a thermoelectric stage (in contrast to resistive heaters)[39] that can alternate between T_{cold} and T_{hot} in < 5 min. The fast cycling allows averaging the change in reflectance over multiple cycles in an effort to reduce the large noise associated with steady state TTI. Since the experiment is quite sensitive, the acquisition of accurate C_{TH} values is a significant undertaking that requires extensive calibrations.[40] TTI is uniquely able to measure both metallic (unlike Raman) and nonmetallic structures with the appropriate choice of excitation wavelength.[41] Gold metallic

structures (such as transistor gates) are well measured with 470 and 530 nm light sources,[42] but the resolution of thin gate structures (gate lengths on the order of 100 nm in RF devices) can be diffraction limited. The same experimental apparatus, with a change in wavelength, may also be capable of measuring the surface of a device channel, allowing complete device thermal maps to be constructed by using multiple probe wavelengths.

B. Gate resistance thermometry (GRT)

In contrast to optical methods, gate resistance thermometry (GRT) is a temperature sensitive electrical parameter (TSEP) method[43] that monitors the change in transistor gate metal resistance with temperature.[44] For relatively wide ranges of temperature (100–500 K), the metallic resistance varies linearly with temperature[45] and can be acquired using a four-wire Kelvin setup (supplying a probe current and measuring the voltage drop across the gate width). Prior to monitoring the *in situ* temperature, the gate metal temperature coefficient of resistance (TCR) is extracted via a calibration with a temperature-controlled stage. Once calibrated, the four-wire resistance measurement can be executed by supplying a probe current during drain and gate biasing. Based on the electrical setup, GRT can capture both the steady state and transient temperature rise in the gate metal temperature with minimal averaging.[44] For GaN high electron mobility transistors (HEMTs), the hotspot is typically located near the drain edge of the gate,[46] which can make the GRT measurement an accurate temperature sensor within close proximity to the peak temperature rise. Specifically, GRT can be advantageous in comparison with other methods when the hotspot is optically restricted by a field plate.[27]

Despite GRT's high throughput, caution must be taken when using this technique to benchmark devices that undergo different processing methods or have different geometries. For long gate widths ($>$ 400 μm), the spatially averaged temperature can under predict the peak temperature by 20%.[47] When comparing on-wafer GRT measurements to substrate thinned packaged devices, the TCR was shown to change by 15%[48] due to a potential change in the chemical composition of the gate metal during packaging. Furthermore, the instability of the TCR has been reported in GaN HEMTs for acquisition periods over a few hours, thus requiring re-calibrations.[49]

C. Raman spectroscopy

Raman spectroscopy is a canonical method for the characterization of phonon vibrational modes. In crystalline materials, the energy and lifetime of these phonon modes can be related to the strain, temperature, and electric field in the crystal.[50] With careful calibration, it is possible to use mathematical techniques to decouple these parameters in a device.[51,52] For device thermal characterization, confocal Raman spectroscopy is used as a point measurement technique by focusing a laser (beam diameter size $\approx$1 μm) near the device's hotspot (dependent on optical access). However, high photon densities are required to induce Stokes and anti-Stokes scattering events in detectable quantities, which can impact the device's carrier transport.[53] Long acquisition times are thus typically implemented to minimize the impact of the laser on carrier excitation or avoid laser-induced heating in some cases.[54] This limitation has made large area temperature mapping studies[51] or lock-in transient measurements[55] severely time consuming (in addition to requiring an efficient method for high throughput curve fitting). Nevertheless, Raman thermometry has demonstrated accurate peak temperature evaluation in UWBG heterogeneous structures,[56–58] and high-throughput methods are making rapid developments[31] that may be applied for thermal mapping in the next decade.

Other challenges faced by Raman thermometry included depth averaging over thick epitaxial layers due to sub-bandgap excitation sources.[15] For example, thick buffer layers (5 μm) are typically required for GaN on Si substrate HEMTs. The device temperature extracted from the GaN phonon frequency for the structures has been reported to under predict the peak (surface) temperature by 40%.[59] Moreover, the challenge with depth averaging has been encountered in UWBG devices, such as gallium oxide or diamond,[60] where the active channel is homoepitaxially grown on a native substrate. The deposition of Raman-active nanoparticles[61] or 2D materials[62] to act as surface temperature transducers has been developed to overcome these challenges and provide an accurate surface temperature measurement. However, conformal and uniform nanoparticle deposition across the device topography and dissimilar material surfaces has proven challenging for high spatial resolution mapping.[59]

D. Scanning thermal atomic force microscopy (SThM)

Scanning thermal atomic force microscopy employs a thermal probe affixed to the end of an atomic force microscope probe to map temperature gradients and thermal conductivity across a device surface.[63–65] This technique was initially developed using a Wollaston wire and later developed with the introduction of palladium thermistors (measuring a change in resistance due to a change in temperature). Both of these technologies, however, faced challenges when probing areas with active current since direct contact with the metal tip would cause electrical interference. Recent advances in designing SThM tips has reduced the electrical contact area by depositing an SiO_2 thermal insulating layer below an integrated a sub-micron scale thermocouple.[66] By mapping the temperature distribution at the scales beyond the diffraction limit, SThM provides very detailed insight into surface thermal behavior. Although SThM offers unparalleled spatial resolution (50 nm),[67] its contact-based nature can affect quantitative measurements and the applicability of the method may vary depending on the thermal conductivity of the material, as the tip can act as a heat sink, altering the thermal profile.[68] Other scanning probe techniques, such as scanning joule expansion microscopy,[69,70] have been developed simultaneously for device thermal mapping. These techniques accurately generate thermal distribution profiles but face challenges in quantifying accurately the temperature rise.

III. CHALLENGES IN TTI FOR UWBG MATERIALS

Traditional, commercially available TTI systems have relied on the strong reflectance of gate metals in transistors to estimate the device peak temperature rise. Typical gate lengths, however, can reach down to 100 nm (designed for RF applications), which can restrict the use of TTI due to its diffraction-limited spatial resolution. Channel temperature measurements, via direct thermoreflectance of the semiconductor channel, must thus be used to estimate the peak temperature. Moreover, probing the active channel surface temperature will unlock the true potential of TTI's high throughput spatial and temporal mapping. The physical mechanism by which photon reflection at a semiconductor surface occurs is a significant challenge in TTI, especially in the exploration of UWBG semiconductors. The photon

wavelength is proportional to the energy of the photon, and complete reflection from the top surface is not expected to occur if the energy of the incident photon does not meet or exceed the energy of an electron state transition. These sub-bandgap photons transmit through materials with partial reflection and some transmission.[71] As the layers of these devices are quite thin, this can result in Fabry–Pérot (thin-film) interference patterns. Photons with energy in excess of the bandgap energy will reflect,[41] but they will also impart energy into the material, which may excite additional carriers. The consequences of optical carrier excitation may range from device damage to poor experimental control.[7]

The necessity of bandgap-photon energy matching possesses significant technical challenges for UWBG materials.[72] The well-known relationship between photon energy and wavelength allows for easy calculation of the required light source via the classic equation $\lambda = hc/E_0$. In a UWBG material, the bandgap energies correspond to wavelengths in the deep-UV range of the optical spectrum. For example, $\beta - Ga_2O_3$ has a bandgap of approximately 4.8 eV, which corresponds to a wavelength of approximately 258 nm. However, the commercial availability of deep-UV light sources and optical elements (mirrors, lenses, etc.) is poor, and it is important to consider alternative approaches to near-bandgap TTI.

IV. FUTURE DEVELOPMENTS IN TTI AND OTHER THERMAL CHARACTERIZATION TECHNIQUES

A. Hyperspectral TTI

Inspection of Eq. (1) suggests that another measurement can be made using the change in surface reflectivity (under biasing) and C_{TH}. In particular, if multiple independent values of C_{TH} and changes in $\Delta R/R$ are measured, the change in temperature should be the slope of the linear relationship between the two measured quantities. C_{TH} is not directly controllable, but by changing the wavelength of the incident light source, it can be indirectly adjusted. This type of measurement is known as a hyperspectral TTI (HTTI) measurement,[73,74] and it offers many advantages over a traditional TTI measurement at the expense of experimental complexity.

Primarily, HTTI's measurement accuracy does not depend solely on a strong reflected light signal. Due to the noise associated with TTI calibrations, the temperature map acquired from a traditional single excitation wavelength requires an external verification. The temperature could be verified by an alternative method in combination with numerical modeling: Raman for the channel temperature[33] and GRT for the gate metal temperature. If the user has a limited setup, however, a secondary probe wavelength is used to acquire a TTI map and a C_{TH}. The images are considered accurate when close agreement is observed between the temperatures acquired by independent wavelengths.[75,76] The dual wavelength approach faces setbacks if there are temperature discrepancies between the two wavelengths or if there is simply not a secondary wavelength available that outputs a strong thermoreflectance signal (a primary concern for the acquisition of the channel temperature). Furthermore, even with close agreement in temperatures, the user would not know if there is a systematic offset in the temperature values. By using three or more wavelengths, the HTTI approach can be externally verified by ensuring a good linear fit that crosses the origin. A significant variation in the $\Delta R/R$ quantity between different wavelengths is helpful for having a well-defined and fitting friendly relationship.[73,74]

For the purpose of demonstrating a hyperspectral study, a single finger AlGaN/GaN-based HEMT integrated on a diamond substrate with a thin SiN interlayer was fabricated and is shown in Fig. 1(a).[77,78] Figure 1(a) also shows the reflection paths expected of a bandgap matching surface reflection and a sub-bandgap reflection dominated by Fabry–Pérot interference. The device geometry featured a 75 μm gate width (W_g) and 3 μm gate length (L_g). The gate to drain spacing was 10 μm, and the channel spacing (L_{CH}) was 15.5 μm. GaN, with a bandgap of $\approx$3.4 eV, has a corresponding wavelength match at approximately 365 nm, although the bandgap is sensitive to stresses developed in the manufacturing processes.[23,79] Four series of TTI measurements were conducted using wavelengths of 365, 385, 470, and 530 nm. The 365 nm wavelength is used as a reference in order to verify the hyperspectral measurement. These measurements were performed at the region of interest (ROI_1) indicated in green in Fig. 1(b). The red "Gate ROI" (ROI_2) was also analyzed, and the results of the HTTI analysis are included in the supplementary material. In all measurements, the devices were operated with a power density of 5.4 W/mm at $V_{GS} = 1$ V with a 400 μs pulse width and a 20% duty cycle. The drain-source voltage (V_{DS}) was adjusted during each measurement to maintain a constant power density across all wavelengths (in the range of 12.8–13.75 V). Small changes in the drain bias (<1 V) were assumed to have an insignificant impact on the Joule heating profile.

The thermoreflectance spectrum for the GaN channel ROI_1 confirms a strong thermoreflectance signal originating from sub-bandgap wavelengths [Fig. 1(c)]. The reflected light, measured by the CCD, is governed by Fabry–Pérot interference, which can be approximated as a combination of the surface temperature and depth-averaged temperature.[80] There is a small reflection at the upper surface and another at the AlGaN/GaN interface, and the interference between the reflections is governed by the optical path length. As the device heats up, this path length changes due to thermal expansion, which produces a temperature dependent reflectivity and facilitates the use of thermoreflectance methods.[80] The effects of depth averaging are expected to be minimal in this case due to the thickness of the layer being far below 700 nm.[78]

For the ROI_1 shown in Fig. 1(b), it is possible to extract the values of $\Delta R/R$ and C_{TH} for each wavelength, and those values are shown for the 385, 470, and 530 nm wavelengths in Fig. 1(d). Within ROI_1, the temperature rise is evaluated from the slope of a linear fit of the $\Delta R/R$ and C_{TH} relationship and in this case is 15.44 $\pm$ 0.63 °C.

Considering the whole channel, as shown in Fig. 2(a), it is possible to perform this hyperspectral analysis for the entire field of view with an advanced piezoelectric stage for autofocusing and pixel alignment.[81] After performing a pixel-by-pixel alignment of the optical CCD images, Figs. 2(b) and 2(c) show the magnitudes of $\Delta R/R$ and C_{TH} maps at probe wavelengths of 385, 470, and 530 nm, respectively, with identical spatial locations for each pixel. For each wavelength excitation, C_{TH} and $\Delta R/R$ values are thus known for each pixel and the HTTI analysis may be performed on a pixel-by-pixel basis. After this careful pixel-by-pixel alignment, Fig. 2(d) shows the resultant temperature field from the hyperspectral linear fit. The hyperspectral image is subsequently compared with the thermal image obtained via near bandgap thermoreflectance using a 365 nm LED [Fig. 2(e)]. Good agreement is seen with less than 5% difference. The marginally higher temperatures observed in the 365 nm map are attributed to the near bandgap TTI being predominantly a surface temperature measurement, whereas the sub bandgap HTTI represents a weighted depth-averaged temperature.

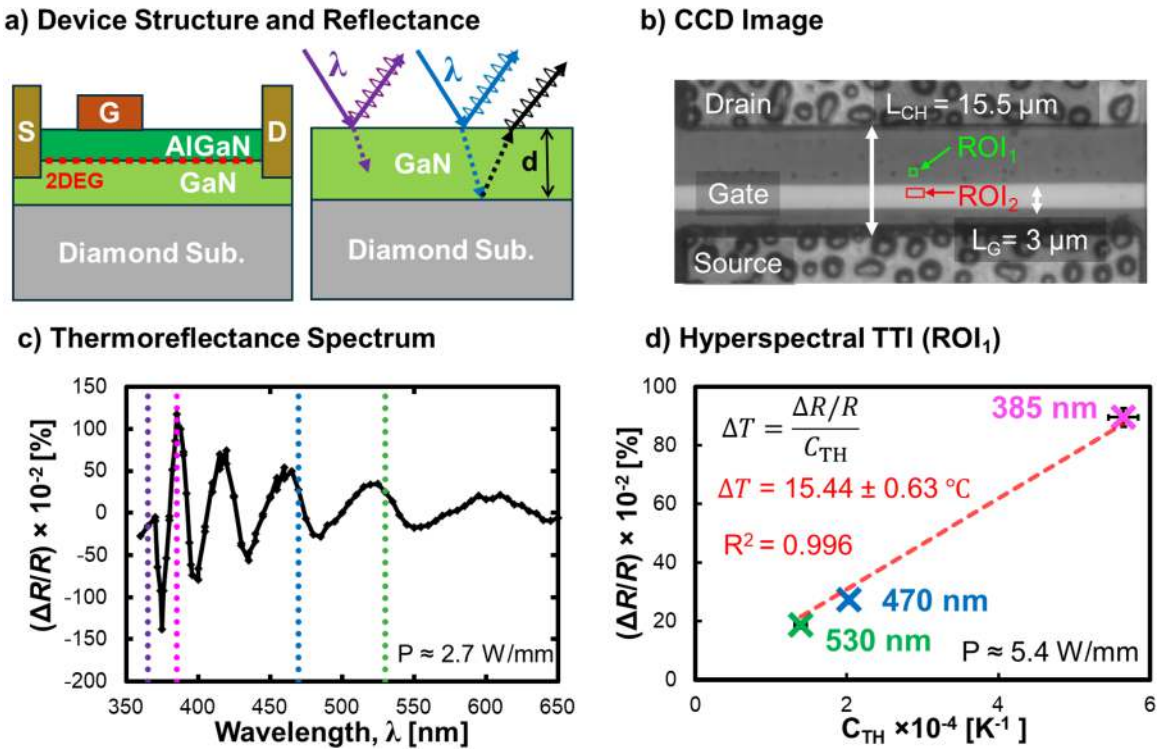

FIG. 1. (a) A simplified schematic of redan AlGaN/GaN HEMT (left) on thick CVD diamond substrate that was thermally characterized using transient thermoreflectance imaging (TTI) for different probe wavelengths (λ). A simplified schematic of the GaN on a diamond transmission/reflection system (right) showing a surface level, bandgap matched reflection, and a multisurface reflection, which gives rise to Fabry–Pérot interference. (b) Optical CCD image of the device featuring the channel length (L_{CH}) and the gate length (L_G). The region of interest (ROI_1), represented as a green square, was used to extract the thermoreflectance coefficient (C_{TH}) and the reflectance change ($\Delta R/R$). (c) Steady state thermoreflectance spectra of the device while operating at a power density (P) of 2.7 W/mm. (d) Temperature measurement of ROI_1 based on the linear fit of the hyperspectral TTI method. The thermoreflectance response of ROI_1 was recorded for three different wavelengths (385, 470, and 530 nm) at $P = 5.4$ W/mm and plotted against C_{TH} calibrated for each wavelength.

Regarding the corresponding R-squared (R^2) values of the fit, the R^2 map can be used to determine the successful implementation of HTTI for different regions (a verification method that is not possible with a single wavelength). The region of low R^2 in the channel, depicted in Fig. 2(d), is correlated with a region of irregular C_{TH} and $\Delta R/R$ seen in the 385 nm wavelength. In this region, the 385 nm wavelength did not give a strong reflection, which is possibly attributed to the presence of defects (a phenomenon discussed in Sec. IV B). Based on Fig. 2(d), the largest area with a consistently high R^2 (>0.9) corresponds to the upper half region of the channel. The temperature distribution across the channel is therefore extracted from the upper half to compare the HTTI channel temperature profile to the individual probe wavelengths [Fig. 3(a)]. As expected, the peak temperature is located near the gate edge on the drain side. The gate temperature profile obtained from the 470 and 530 nm LED is plotted in Fig. 3(a) (wavelengths that have historically shown good accuracy for gold). The continuity in temperature distribution across the gate metal and channel further verifies the accuracy of using hyperspectral imaging to evaluate the channel temperature of WBG and UWBG semiconductors.

In addition to mapping the temperature distribution, a transient sweep was performed to further understand the temperature dependency of the sub-bandgap thermoreflectance. To increase the signal to noise ratio, a fourth additional sub-bandgap wavelength was implemented (415 nm). Figure 3(b) depicts the transient thermal profile for a 1 μs drain pulse dissipating 5.4 W/mm at a 15% duty cycle. The temperature was extracted at the 8.6 μm position along the line described in Fig. 3(a). The shorter pulse width enabled faster temporal resolution (50 ns), which is required to detect any subtle differences between the different wavelengths. Consequently, the shorter pulse width also reduced the time for cooling between consecutive pulses, which caused heat accumulation in the OFF state.[82] The increased reference state temperature thus resulted in a 20% lower peak temperature. Nevertheless, the 1 μs transient sweep enabled a direct comparison of the 365 nm transient response compared to the sub-bandgap HTTI. The two datasets overlap significantly; however, the 365 nm results in 14% higher peak temperature near the end of the pulse. The increase in temperature confirms the hypothesis that sub-bandgap TTI is not a true surface temperature measurement.

Figure 3(c) portrays the channel temperature profile along the gate width at a distance of 1 μm away from the drain side of the gate metal [origin shown in Fig. 2(a)]. The 530 nm reading shown in Fig. 3(c) represents the nearby gate metal temperature and confirms the symmetric distribution of temperature along the gate width as shown in the channel. In this case, it is clear that the hyperspectral

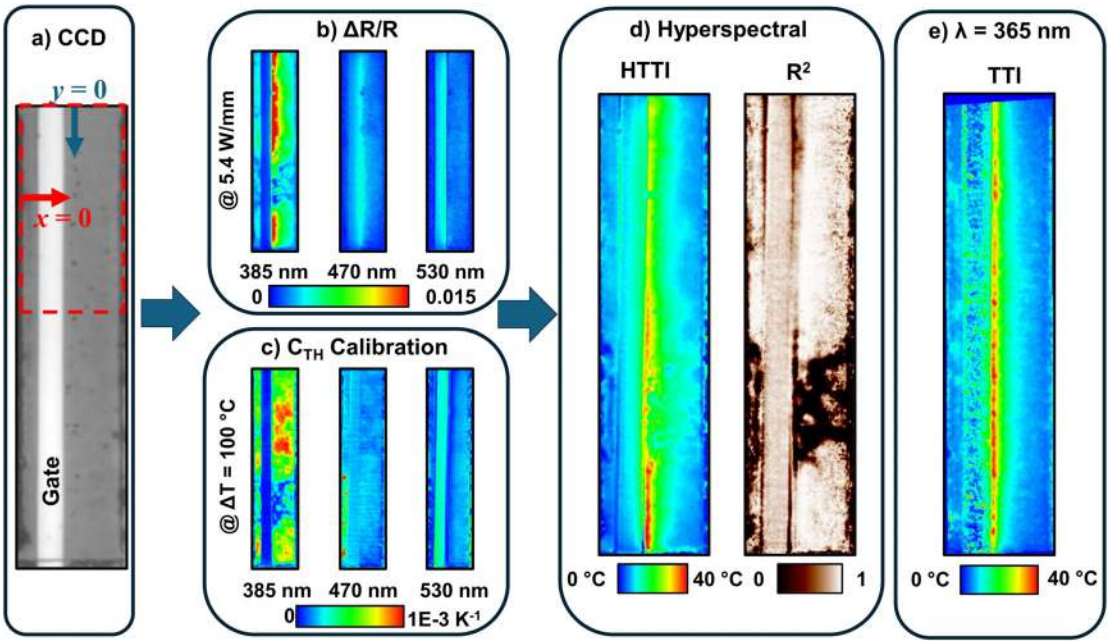

FIG. 2. (a) Optical CCD image of the device's channel and gate metal studied with transient thermoreflectance imaging (TTI). (b) Map of absolute value of reflectance change, $\Delta R/R$, measured during TTI with a 385, 470, and 530 nm LED. A 400 μs pulse width with a 20% duty cycle was applied to the device while maintaining a constant $V_{GS} = 1$ V. The average power density was 5.4W/mm, and the thermal images were averaged over the last 25 μs of the pulse. (c) Map of absolute thermoreflectance coefficient, C_{TH}, for the given excitation wavelengths. The calibrations were calculated based on a temperature rise of 100 °C. (d) Computed hyperspectral transient thermoreflectance image (HTTI) and corresponding R^2 map. (e) Reference temperature map using a 365 nm LED, which is a bandgap match and expected to give an accurate surface temperature.

result closely matches the nearby 530 nm result on the gate metal, and regions corresponding to elevated error in the 365 and 385 nm component signals nevertheless show the expected behavior in the HTTI result. This noise insensitivity is due to the tendency of a linear data fit, which is performed as a part of the HTTI data processing, to minimize the effects of outliers. In regions where a component signal is carrying significant noise content, the HTTI result is expected to be more accurate when the R^2 value is high and the $\Delta R/R$ vs C_{TH} relationship has a y-intercept near to zero [see Fig. 1(d) for a representative plot of this type].

In summary, the HTTI method is very well suited for cases where photon-induced currents are particularly undesirable because it can be executed entirely with sub-bandgap wavelengths. While the HTTI method is significantly more work than the use of a single sub-bandgap source for TTI, it has the advantage of providing two mechanisms for error checking and estimating. The first is that by checking for the y-intercept of the HTTI fits, regions where the intercept is not near zero may be identified as being suspect and can be addressed. The second, is that by providing an R^2 map, the fit quality may be used to evaluate the accuracy of the measurements spatially. It is also possible to use the fitting process to provide a true error bound estimate, rather than depending on statistics on the pixels in an assumed-to-be-uniform temperature ROI.

B. Sub-bandgap TTI

Historically, it has been assumed that the thermoreflectance signal from a semiconductor originates from the photon–electron shell interaction occurring only at the bandgap energy between the semiconductor's conduction and valence bands.[15] This has been supported by experimental work on GaN HEMTs, which has shown near-bandgap TTI channel measurements agree with the gate metal surface temperatures.[41] However, previous work has also reported a notable thermoreflectance signal from both GaN and gallium oxide with sub-bandgap excitation sources,[81,83] as also shown in Figs. 1(c) and 4(a). There are likely at least two mechanisms by which sub-bandgap thermoreflectance methods may be applied. In the first case, there are heteroepitaxial, thin film structures, which use Fabry–Pérot interference patterns as the governing mechanism. In the second case, there are methods based on the measurement of other electron transitions in the channel, namely, in this case, channel material defect transitions, which may be used for some homogeneous structures.

In the case of WBG devices grown on non-native substrates, such as the device in Fig. 1(c), the thermoreflectance spectra typically demonstrate multiple oscillations, which originate from Fabry–Pérot interference patterns.[15,80,85,86] The accuracy of the estimated surface temperature, derived from the sub-bandgap thermoreflectance image, is highly dependent on the layer thicknesses. In particular, internal reflections across thick buffer layers (e.g., 5 μm) reduce the signal to noise ratio (due to a lower C_{TH}[87]) and ultimately underestimate the true surface temperature. On the other hand, as shown in Fig. 3(a), sub-bandgap probe wavelengths can approximate the channel temperature for devices with thin buffer layers (<1 μm). Since the bandgap of a semiconductor is highly stress dependent, a fixed probe wavelength may create a thermoreflectance image composed of both near bandgap and sub bandgap regions with significantly different C_{TH}'s. As

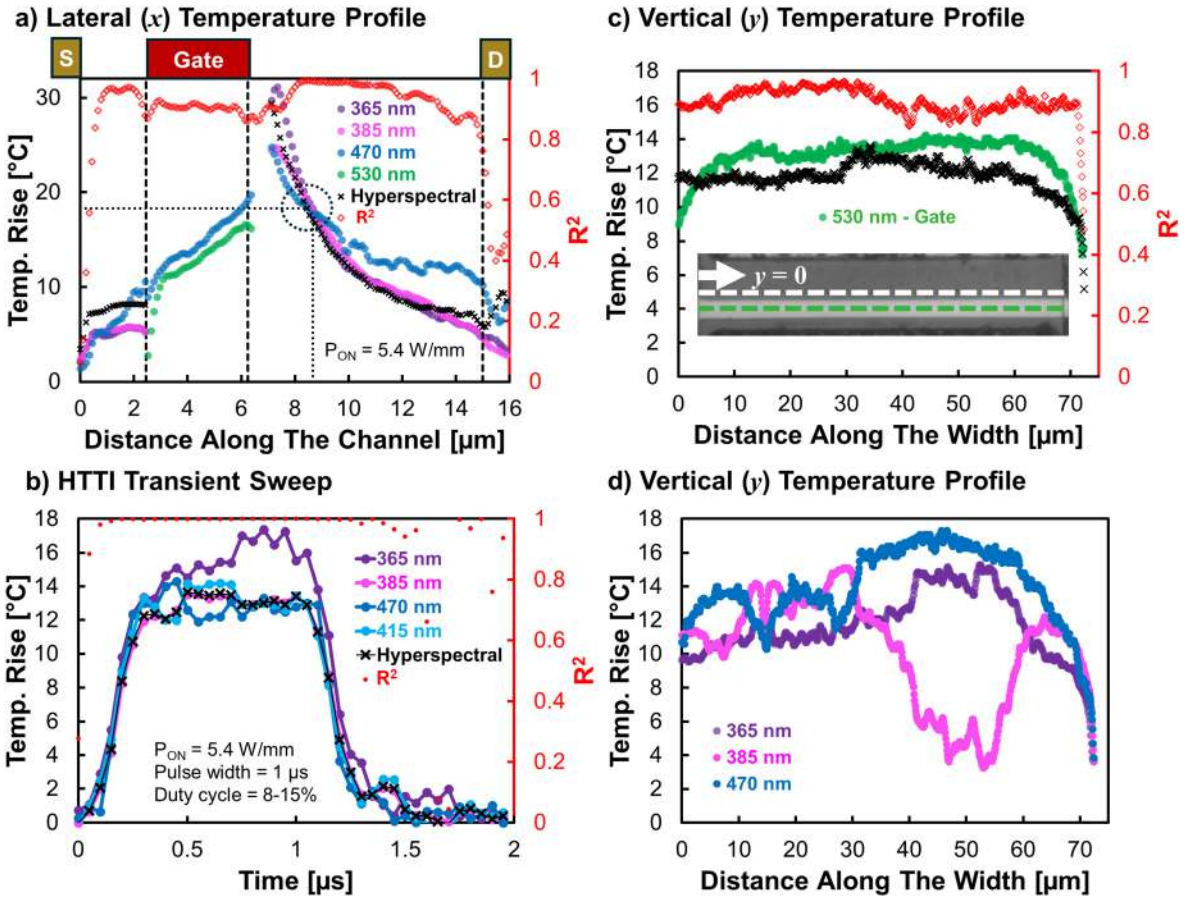

FIG. 3. (a) Extracted temperature profile across the GaN channel (x axis) corresponding to the column averaged upper half of Fig. 2(a) (red dashed rectangle). The HTTI temperatures are evaluated with the 385, 470, and 530 nm wavelengths, and a 365 nm temperature rise profile is shown for comparison. The temperature profile across the gate metal is shown for a 530 and 470 nm excitation, but 365 and 385 nm are not shown on the metal due to the poor reflectivities of those wavelengths. The R^2 values of the HTTI fit are shown in red on the right vertical axis. (b) HTTI transient profile (evaluated with 385, 470, and 415 nm) over a device power cycle, averaged over approximately 5200 cycles at each time step (50 ns). The region of interest is located along the same line as the profile of Fig. 3(a) at the 8.6 μm position. (c) HTTI (evaluated with 385, 470, and 530 nm) temperature distribution along the channel width (y axis). The profile is extracted 1 μm away from the gate metal [coordinate shown in Fig. 2(a)]. The R^2 values of the HTTI fit are shown in red on the right vertical axis. An additional cross section temperature profile of the gate metal, using a 530 nm LED, is shown for comparison. (d) Temperature profile along the channel width for 385 and 470 nm excitation, which is used for HTTI analysis. The temperature profile acquired from 365 nm excitation is shown for comparison.

mentioned in Sec. IV A, the spatial variation of C_{TH} can be accounted for with a pixel-by-pixel calibration (likewise the uncertainty of C_{TH} can be reduced through the hyperspectral approach).

Previous thermal studies on UWBG devices with homoepitaxial layers, such as gallium oxide, have shown thermoreflectance spectra with different behavior[83] [Fig. 4(a)]. For the gallium oxide device analyzed, the Ga_2O_3 epilayers were homoepitaxially grown,[83] and so Fabry–Pérot interference is unlikely to occur due to the lack of a distinct material transition, suggesting an alternative mechanism for sub-bandgap thermoreflectance.

In the gallium-oxygen system, there are more possible electron transitions than the valence-conduction band transition typically considered in a semiconductor material system. Some sources, in discussion of UID gallium oxide, suggest the presence of defect gallium acceptors and defect oxygen donors by experiment[84] with theoretical support provided by the density functional theory (DFT) and tight-binding models where they are addressed as inter-subband transitions.[88] Other experiments, considering Fe^{3+} and Cr^{3+} doped gallium oxide systems, show electron transitions related to exchanges in and out of the impurities.[89] The thermoreflectance spectra shown in Fig. 4(a) show a high degree of sensitivity in the vicinity of 470 nm,[83] which corresponds to the energy levels associated with defect-based UID gallium oxide electron transitions associated with quantum wells formed by clusters of gallium acceptor defects.[84,88,90,91]

Despite the presence of aluminum doped surface layers and an iron doped substrate layer, this device does not show the characteristic activity peaks at 690, 696, and 709 nm associated with Fe^{3+} doping[89] as shown in Fig. 4(a) or any other regions of high activity, which might be attributed to the aluminum. This suggests that the aluminum alloying content might not be sufficient to produce a measurable effect, or

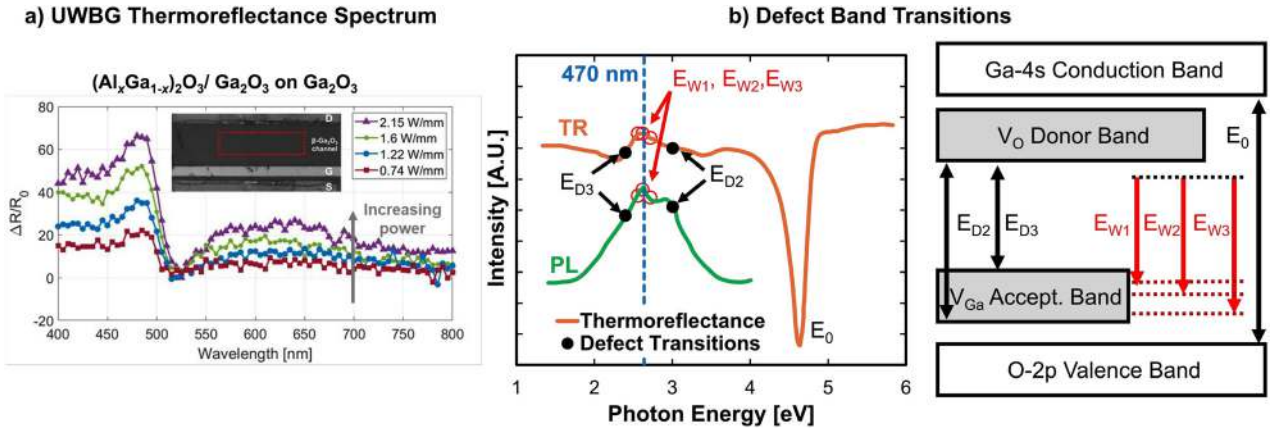

FIG. 4. (a) Thermoreflectance spectra for a gallium oxide device reproduced from a previous publication on this device.[83] (b) Comparison of photoluminescence (PL) intensity and thermoreflectance (TR) spectra, at 300 K, highlighting the presence of increased sensitivity in the regions defined by the conduction-valence bandgap E_0 and defect electron transitions E_{D2} through E_{D3}, including the quantum well transition family E_W adapted from Ref. 84 with additional emphasis.

does not do so, but additional experimentation is necessary to confirm this hypothesis. Alternatively, the iron doping in the substrate may not be sufficiently homogeneous to create a broadly detectable TTI signal, as is shown in Remple *et al.*,[89] where the iron and chromium impurities structures are active in photoluminescence experiments, but the emissions are localized to dopant clusters.

As shown schematically in Fig. 4(b), the active electronic transitions in addition and the main bandgap, E_0, are shown. The corresponding band diagram is shown in Fig. 4(c). These transitions result from the interactions between a gallium defect acceptor band and an oxygen defect donor band. Two of them, E_{D2} and E_{D3}, are simple transitions between the donor and the defect acceptor bands. The third, E_W, is a set of transitions within a quantum well formed by shared vacancies in the gallium-oxygen system and the defect donor band. The photoluminescence results shown in Fig. 4(b) show good agreement between the thermoreflectance spectra $\Delta R/R$ and the photon emissions from these electron transitions.[84,88,89,92]

While the temperature extracted from sub-bandgap TTI (λ=470 nm) of $(Al_xGa_{1-x})_2O_3/Ga_2O_3$ HFETs has shown good agreement with the gate metal temperature,[83] the thermal characterization of n-type Ga_2O_3 field-effect transistors resulted in severe temperature underestimations.[93] Given the proximity of the gallium-oxygen defect transitions to the probing wavelengths in these studies, further investigation is needed to characterize the defect concentrations in both of these structures and relate it to the intensity of the thermoreflectance signal. Nevertheless, sub-bandgap TTI could still be fruitful for lower defect systems if systematic calibrations were applied via numerical simulations. Furthermore, alternative characterization methods [such as PL in Fig. 4(b)] could be used to characterize these electron transitions and further develop sub-bandgap TTI as deep-ultraviolet (DUV) optics (for near bandgap TTI) remain power-limited.

C. Advancements in TTI for UWBG applications: DUV optics

To address near bandgap TTI for UWBG devices, a deep ultraviolet (DUV) LED-based TTI optical microscope is currently being optimized for 265 nm (4.68 eV) transmission.[72] Schematically shown in Fig. 5, the microscope uses optical elements (collimator, beam splitter, and polarizer) from commercial sources. The system currently faces two limiting elements. The first is the LED intensity, which has a 55 mW output power, but it is reasonable to expect higher powers to become available with future investments.[94] UWBG semiconductors materials are an enabling technology for the improvement of DUV optoelectronics, and there is significant commercial and scientific interest in the development of higher power LEDs and other optical elements for this spectral region.[1] As previously mentioned, photon-induced currents are possible in near-bandgap measurements. However, one can reduce this risk by using collimated, low power LED light sources, or a uniformly expanded and collimated laser source. In contrast to a highly localized illumination of a laser, diffuse lighting on the device's surface will minimize any potential differences within the device, though a potential difference may still exist across the wafer.

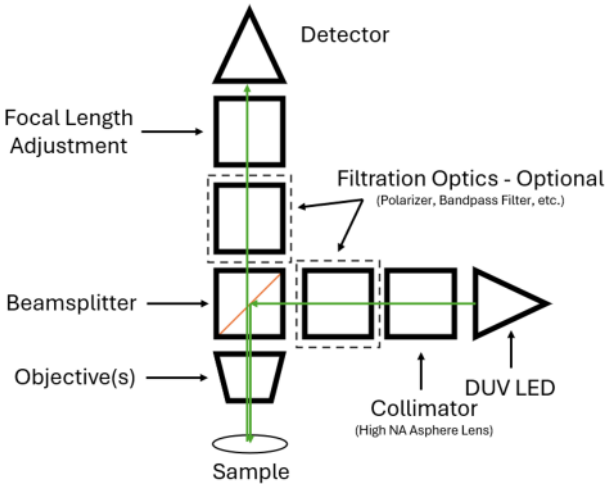

FIG. 5. Schematic of DUV TTI Microscope. Optional elements shown are currently being experimentally developed.

With careful administration of the light source intensity and monitoring of the detected signal strength, the photon-induced currents may be kept to a practical minimum.[35] It is good practice to monitor the health of the devices under test by analyzing the device transfer curve before, during, and after testing to assess for damage.

The second challenge associated with the DUV microscope is the beam splitter, which is used to allow for the passage of incident and returned light. In all commercially available TTI microscopes, the beam splitter is used to bring the probe light onto the optical axis, while still allowing the reflected light to reach the detector.[15,16] A true 50–50 splitting element is used, and since the light emitted from the LED must ultimately pass through the splitting element twice to reach the detector, approximately 75% of the potential signal strength is lost.

Two optional elements are shown in the schematic, which are currently being used to evaluate the advantages of using polarization to permit more total light throughput. It is hypothesized that if a beam-splitting element is used, which reflects only polarized light at high efficiency, a polarized light source may be introduced into the optical path with a low loss of useful light. Diffuse reflections are generally depolarized to a high degree, so the returned light would be rejected at approximately a 50% rate, and the total light throughput to the detector would be closer to 50% than 25% in the current state-of-the-art. With the relatively low power output from commercially available DUV LEDs, the increased optical efficiency of the system may justify the increased complexity if polarized light sources are available in the near future.

V. CONCLUSION

UWBG semiconductors offer many challenges and opportunities. The superior electronic properties of UWBG materials, such as gallium oxide, AlN, AlGaN, and diamond, make them indispensable candidates for high-power and high-frequency electronics applications. For gallium oxide and AlGaN, one challenge for their adoption are constraints imposed by low thermal conductivity and localized heating phenomena. For example, the native substrate thermal conductivity (11–27 $Wm^{-1}K^{-1}$) of $\beta - Ga_2O_3$ limits vertical device development.[12] The development of UWBG semiconductor devices continues to drive further advances in thermal metrology techniques, and new technologies are emerging to meet the challenges outlined in this perspective.

GRT, Raman spectroscopy, and SThM are mature technologies, and all offer unique advantages and will remain critical tools. TTI, with its many advantages and challenges, will also continue to adapt to the unique challenges of UWBG materials and devices. Hyperspectral TTI offers tremendous potential for the characterization of UWBG materials using sub-bandgap optical sources in this period where DUV optics remain technologically and commercially limited. Hyperspectral TTI measurements are challenging to execute compared to traditional TTI methods, requiring exceptional image alignment across many imaging sessions and optical source changes, but when successfully executed offer good results as demonstrated with a WBG GaN case study. The development of machine learning algorithms for thermal imaging could improve the throughput of HTTI measurements and reduce the uncertainly of pixel alignment.[95]

There is a tremendous opportunity to explore the use of other electron state shifts for performing sub-bandgap TTI. Complex semiconductor material systems, such as gallium oxide with its six phases and numerous alloys, demonstrate other photon–electron interactions, which may be exploited for thermal metrology purposes. Deeper understanding of these other photon–electron interactions, and calibration of systems to accurately measure those transitions while rejecting others, is an avenue for future work that offers a significant potential.

In parallel to the development of sub-bandgap TTI methods, it is likely that DUV optical technology will also continue to mature. At present, it is possible to perform TTI measurements of UWBG materials directly if the low intensity of the light is properly accounted for. It is highly probable that the availability of DUV LEDs will improve in time. The adoption of UWBG material-based technology is directly linked to the development of improved optoelectronics[1] in a manner, which is self-reinforcing—as adoption and understanding of the materials grows so too will the availability of optical sources in the DUV range of the spectrum, which can be leveraged to perform TTI.

SUPPLEMENTARY MATERIAL

See the supplementary material for discussion of the hyperspectral analysis on the gate metal of this AlGaN/GaN HEMT contrasted with the channel.

ACKNOWLEDGMENTS

Research at the Naval Research Laboratory was supported by the Office of Naval Research. GaN on Diamond Devices were fabricated during the sponsorship of Dr. Georges Pavlidis in the 2024 ONR Summer Faculty Research Program at the Naval Research Lab. Dominic Myren was supported by the Department of Defense (DoD) through the National Defense Science and Engineering Graduate (NDSEG) Fellowship Program.

AUTHOR DECLARATIONS

Conflict of Interest

The authors have no conflicts to disclose.

Author Contributions

D. Myren: Investigation (equal); Methodology (equal); Writing – original draft (lead); Writing – review & editing (equal). **F. Vásquez-Aza:** Data curation (equal); Formal analysis (supporting); Investigation (equal); Methodology (equal); Writing – original draft (equal). **J. S. Lundh:** Data curation (equal); Supervision (equal); Writing – original draft (supporting); Writing – review & editing (supporting). **M. J. Tadjer:** Funding acquisition (equal); Project administration (equal); Writing – original draft (supporting); Writing – review & editing (supporting). **G. Pavlidis:** Conceptualization (equal); Data curation (equal); Formal analysis (equal); Funding acquisition (equal); Investigation (equal); Methodology (equal); Project administration (equal); Resources (equal); Supervision (equal); Writing – original draft (equal); Writing – review & editing (lead).

DATA AVAILABILITY

The data that support the findings of this study are available from the corresponding author upon reasonable request.

REFERENCES

[1]J. Y. Tsao, S. Chowdhury, M. A. Hollis, D. Jena, N. M. Johnson, K. A. Jones, R. J. Kaplar, S. Rajan, C. G. Van De Walle, E. Bellotti, C. L. Chua, R. Collazo, M. E. Coltrin, J. A. Cooper, K. R. Evans, S. Graham, T. A. Grotjohn, E. R. Heller, M. Higashiwaki, M. S. Islam, P. W. Juodawlkis, M. A. Khan, A. D. Koehler, J. H. Leach, U. K. Mishra, R. J. Nemanich, R. C. N. Pilawa-Podgurski, J. B. Shealy, Z. Sitar, M. J. Tadjer, A. F. Witulski, M. Wraback, and J. A. Simmons, "Ultrawide-bandgap semiconductors: Research opportunities and challenges," Adv. Electron. Mater. **4**, 1600501 (2018).

[2]M. Xu, D. Wang, K. Fu, D. H. Mudiyanselage, H. Fu, and Y. Zhao, "A review of ultrawide bandgap materials: Properties, synthesis and devices," Oxford Open Mater. Sci. **2**, itac004 (2022).

[3]Y. Qin, B. Albano, J. Spencer, J. S. Lundh, B. Wang, C. Buttay, M. Tadjer, C. DiMarino, and Y. Zhang, "Thermal management and packaging of wide and ultra-wide bandgap power devices: A review and perspective," J. Phys. D: Appl. Phys. **56**, 093001 (2023).

[4]A. Abdolhosseinzadeh and N. Donmezer, "Thermal spreading resistance of surface adjacent localized heating-induced size effects in semiconductors," J. Electron. Packag. **146**, 041108 (2024).

[5]J. S. Lundh, B. Chatterjee, Y. Song, A. G. Baca, R. J. Kaplar, T. E. Beechem, A. A. Allerman, A. M. Armstrong, B. A. Klein, A. Bansal, D. Talreja, A. Pogrebnyakov, E. Heller, V. Gopalan, J. M. Redwing, B. M. Foley, and S. Choi, "Multidimensional thermal analysis of an ultrawide bandgap AlGaN channel high electron mobility transistor," Appl. Phys. Lett. **115**, 153503 (2019).

[6]S. Choi, E. R. Heller, D. Dorsey, R. Vetury, and S. Graham, "The impact of bias conditions on self-heating in AlGaN/GaN HEMTs," IEEE Trans. Electron Devices **60**, 159–162 (2013).

[7]J. Yang, K. Liu, X. Chen, and D. Shen, "Recent advances in optoelectronic and microelectronic devices based on ultrawide-bandgap semiconductors," Prog. Quantum Electron. **83**, 100397 (2022).

[8]S. Choi, S. Graham, S. Chowdhury, E. R. Heller, M. J. Tadjer, G. Moreno, and S. Narumanchi, "A perspective on the electro-thermal co-design of ultra-wide bandgap lateral devices," Appl. Phys. Lett. **119**, 170501 (2021).

[9]J. B. Casady and R. W. Johnson, "Status of silicon carbide (SiC) as a wide-bandgap semiconductor for high-temperature applications: A review," Solid-State Electron. **39**, 1409–1422 (1996).

[10]Q. Zheng, C. Li, A. Rai, J. H. Leach, D. A. Broido, and D. G. Cahill, "Thermal conductivity of GaN, ^{71}GaN, and SiC from 150 K to 850 K," Phys. Rev. Mater. **3**, 014601 (2019).

[11]G. A. Slack, L. J. Schowalter, D. Morelli, and J. A. Freitas, "Some effects of oxygen impurities on AlN and GaN," J. Cryst. Growth **246**, 287–298 (2002).

[12]Z. Guo, A. Verma, X. Wu, F. Sun, A. Hickman, T. Masui, A. Kuramata, M. Higashiwaki, D. Jena, and T. Luo, "Anisotropic thermal conductivity in single crystal -gallium oxide," Appl. Phys. Lett. **106**, 111909 (2015).

[13]C. E. Quiñones, D. Khachariya, P. Reddy, S. Mita, J. Almeter, P. Bagheri, S. Rathkanthiwar, R. Kirste, S. Pavlidis, E. Kohn, R. Collazo, and Z. Sitar, "High-current, high-voltage AlN Schottky barrier diodes," Appl. Phys. Express **17**, 101002 (2024).

[14]G. A. Slack, R. Tanzilli, R. Pohl, and J. Vandersande, "The intrinsic thermal conductivity of AIN," J. Phys. Chem. Solids **48**, 641–647 (1987).

[15]C. Yuan, R. Hanus, and S. Graham, "A review of thermoreflectance techniques for characterizing wide bandgap semiconductors' thermal properties and devices' temperatures," J. Appl. Phys. **132**, 220701 (2022).

[16]S. Sandell, E. Chávez-Ángel, A. El Sachat, J. He, C. M. Sotomayor Torres, and J. Maire, "Thermoreflectance techniques and Raman thermometry for thermal property characterization of nanostructures," J. Appl. Phys. **128**, 131101 (2020).

[17]J. Zou, D. Kotchetkov, A. A. Balandin, D. I. Florescu, and F. H. Pollak, "Thermal conductivity of GaN films: Effects of impurities and dislocations," J. Appl. Phys. **92**, 2534–2539 (2002).

[18]J. Kuzmík, S. Bychikhin, D. Pogany, C. Gaquière, E. Pichonat, and E. Morvan, "Investigation of the thermal boundary resistance at the III-Nitride/substrate interface using optical methods," J. Appl. Phys. **101**, 054508 (2007).

[19]T. E. Beechem, A. E. McDonald, E. J. Fuller, A. A. Talin, C. M. Rost, J.-P. Maria, J. T. Gaskins, P. E. Hopkins, and A. A. Allerman, "Size dictated thermal conductivity of GaN," J. Appl. Phys. **120**, 095104 (2016).

[20]M. Kuball, S. Rajasingam, A. Sarua, M. J. Uren, T. Martin, B. T. Hughes, K. P. Hilton, and R. S. Balmer, "Measurement of temperature distribution in multifinger AlGaN/GaN heterostructure field-effect transistors using micro-Raman spectroscopy," Appl. Phys. Lett. **82**, 124–126 (2003).

[21]A. Amerasekera, M.-C. Chang, J. Seitchik, A. Chatterjee, K. Mayaram, and J.-H. Chern, "Self-heating effects in basic semiconductor structures," IEEE Trans. Electron Devices **40**, 1836–1844 (1993).

[22]A. J. H. McGaughey, A. Jain, H.-Y. Kim, and B. Fu, "Phonon properties and thermal conductivity from first principles, lattice dynamics, and the Boltzmann transport equation," J. Appl. Phys. **125**, 011101 (2019).

[23]S. Choi, E. Heller, D. Dorsey, R. Vetury, and S. Graham, "The impact of mechanical stress on the degradation of AlGaN/GaN high electron mobility transistors," J. Appl. Phys. **114**, 164501 (2013).

[24]E. Heller, S. Choi, D. Dorsey, R. Vetury, and S. Graham, "Electrical and structural dependence of operating temperature of AlGaN/GaN HEMTs," Microelectron. Reliab. **53**, 872–877 (2013).

[25]G. Pavlidis, A. M. Hilton, J. L. Brown, E. R. Heller, and S. Graham, "Monitoring the Joule heating profile of GaN/SiC high electron mobility transistors via cross-sectional thermal imaging," J. Appl. Phys. **128**, 075705 (2020).

[26]J. Pomeroy, M. Uren, B. Lambert, and M. Kuball, "Operating channel temperature in GaN HEMTs: DC versus RF accelerated life testing," Microelectron. Reliab. **55**, 2505–2510 (2015).

[27]S. Kim, D. C. Shoemaker, A. Karim, H. Walwil, M. T. DeJarld, M. B. Tahhan, J. Vaillancourt, E. M. Chumbes, J. R. Laroche, G. Pavlidis, S. Graham, and S. Choi, "A comparative analysis of electrical and optical thermometry techniques for AlGaN/GaN HEMTs," IEEE Trans. Electron Devices **72**, 162 (2025).

[28]V. Sodan, D. Kosemura, S. Stoffels, H. Oprins, M. Baelmans, S. Decoutere, and I. D. Wolf, "Experimental benchmarking of electrical methods and μ-Raman spectroscopy for channel temperature detection in AlGaN/GaN HEMTs," IEEE Trans. Electron Devices **63**, 2321–2327 (2016).

[29]M. Shahram and P. Milanfar, "Imaging below the diffraction limit: A statistical analysis," IEEE Trans. Image Process. **13**, 677–689 (2004).

[30]X. Zhao, Y. Zhao, S. Hu, H. Wang, Y. Zhang, and W. Ming, "Progress in active infrared imaging for defect detection in the renewable and electronic industries," Sensors **23**, 8780 (2023).

[31]T. Nakamura, K. Hashimoto, and T. Ideguchi, "Broadband coherent Raman scattering spectroscopy at 50,000,000 spectra per second," Ultrafast Sci. **4**, 0076 (2024).

[32]J. Christofferson and A. Shakouri, "Thermoreflectance based thermal microscope," Rev. Sci. Instrum. **76**, 024903 (2005).

[33]S. Martin-Horcajo, J. W. Pomeroy, B. Lambert, H. Jung, H. Blanck, and M. Kuball, "Transient thermoreflectance for gate temperature assessment in pulse operated GaN-based HEMTs," IEEE Electron Device Lett. **37**, 1197–1200 (2016).

[34]X. Zheng, J. W. Pomeroy, G. Jindal, and M. Kuball, "Temperature-dependent thermal impedance measurement of GaN-Based HEMTs using transient thermoreflectance," IEEE Trans. Electron Devices **71**, 2367–2372 (2024).

[35]Y. Mao, H. Zhang, Y. Ma, H. Wang, H. Sun, and C. Yuan, "Multiwavelength laser-based transient thermoreflectance for channel-temperature monitoring of GaN HEMTs," IEEE Trans. Power Electron. **40**, 8648–8657 (2025).

[36]D. G. Pahinkar, P. Basnet, M. P. West, B. Zivasatienraj, A. Weidenbach, W. A. Doolittle, E. Vogel, and S. Graham, "Experimental and computational analysis of thermal environment in the operation of HfO_2 memristors," AIP Adv. **10**, 035127 (2020).

[37]F. Vasquez-Aza, H. Sun, C. Lian, Y.-S. Huang, S. A. Vitale, I. Takeuchi, J. Hu, N. Youngblood, C. A. R. Ocampo, and G. Pavlidis, "Maximizing the thermal performance of microheaters for non-volatile phase change photonics: A comparative study of pulse width parameter effects," in *23rd IEEE Intersociety Conference on Thermal and Thermomechanical Phenomena in Electronic Systems (ITherm)* (IEEE, Aurora, CO, 2024), pp. 1–6.

[38]G. Tessier, S. Holé, and D. Fournier, "Quantitative thermal imaging by synchronous thermoreflectance with optimized illumination wavelengths," Appl. Phys. Lett. **78**, 2267–2269 (2001).

[39]S. Dilhaire, S. Grauby, and W. Claeys, "Calibration procedure for temperature measurements by thermoreflectance under high magnification conditions," Appl. Phys. Lett. **84**, 822–824 (2004).

[40]T. Favaloro, J.-H. Bahk, and A. Shakouri, "Characterization of the temperature dependence of the thermoreflectance coefficient for conductive thin films," Rev. Sci. Instrum. **86**, 024903 (2015).

[41]G. Pavlidis, L. Yates, D. Kendig, C.-F. Lo, H. Marchand, B. Barabadi, and S. Graham, "Thermal performance of GaN/Si HEMTs using near-bandgap thermoreflectance imaging," IEEE Trans. Electron Devices **67**, 822–827 (2020).
[42]K. Maize, G. Pavlidis, E. Heller, L. Yates, D. Kendig, S. Graham, and A. Shakouri, "High resolution thermal characterization and simulation of power AlGaN/GaN HEMTs using micro-Raman thermography and 800 picosecond transient thermoreflectance imaging," in *IEEE Compound Semiconductor Integrated Circuit Symposium (CSICS)* (IEEE, La Jolla, CA, 2014), pp. 1–8.
[43]R. J. T. Simms, J. W. Pomeroy, M. J. Uren, T. Martin, and M. Kuball, "Channel temperature determination in high-power AlGaN/GaN HFETs using electrical methods and Raman spectroscopy," IEEE Trans. Electron Devices **55**, 478–482 (2008).
[44]G. Pavlidis, B. Foley, and S. Graham, "Gate resistance thermometry: An electrical thermal characterization technique," in *Thermal Management of Gallium Nitride Electronics* (Elsevier, 2022), pp. 201–221.
[45]R. A. Matula, "Electrical resistivity of copper, gold, palladium, and silver," J. Phys. Chem. Ref. Data **8**, 1147–1298 (1979).
[46]B. Chatterjee, C. Dundar, T. E. Beechem, E. Heller, D. Kendig, H. Kim, N. Donmezer, and S. Choi, "Nanoscale electro-thermal interactions in AlGaN/GaN high electron mobility transistors," J. Appl. Phys. **127**, 044502 (2020).
[47]G. Pavlidis, S. Pavlidis, E. R. Heller, E. A. Moore, R. Vetury, and S. Graham, "Characterization of AlGaN/GaN HEMTs using gate resistance thermometry," IEEE Trans. Electron Devices **64**, 78–83 (2017).
[48]G. Pavlidis, S. Som, J. Barrett, W. Struble, and S. Graham, "The impact of temperature on GaN/Si HEMTs under RF operation using gate resistance thermometry," IEEE Trans. Electron Devices **66**, 330–336 (2019).
[49]B. M. Paine, T. Rust, and E. A. Moore, "Measurement of temperature in GaN HEMTs by gate end-to-end resistance," IEEE Trans. Electron Devices **63**, 590–597 (2016).
[50]M. Kuball, "Raman spectroscopy of GaN, AlGaN and AlN for process and growth monitoring/control," Surf. Interface Anal. **31**, 987–999 (2001).
[51]S. Choi, E. R. Heller, D. Dorsey, R. Vetury, and S. Graham, "Thermometry of AlGaN/GaN HEMTs using multispectral Raman features," IEEE Trans. Electron Devices **60**, 1898–1904 (2013).
[52]K. R. Bagnall, E. A. Moore, S. C. Badescu, L. Zhang, and E. N. Wang, "Simultaneous measurement of temperature, stress, and electric field in GaN HEMTs with micro-Raman spectroscopy," Rev. Sci. Instrum. **88**, 113111 (2017).
[53]P. B. Klein, J. A. Freitas, S. C. Binari, and A. E. Wickenden, "Observation of deep traps responsible for current collapse in GaN metal–semiconductor field-effect transistors," Appl. Phys. Lett. **75**, 4016–4018 (1999).
[54]O. Lancry, E. Pichonat, J. Réhault, M. Moreau, R. Aubry, and C. Gaquière, "Development of time-resolved UV micro-Raman spectroscopy to measure temperature in AlGaN/GaN HEMTs," Solid-State Electron. **54**, 1434–1437 (2010).
[55]K. R. Bagnall, O. I. Saadat, S. Joglekar, T. Palacios, and E. N. Wang, "Experimental characterization of the thermal time constants of GaN HEMTs via micro-Raman thermometry," IEEE Trans. Electron Devices **64**, 2121–2128 (2017).
[56]B. Chatterjee, J. S. Lundh, Y. Song, D. Shoemaker, A. G. Baca, R. J. Kaplar, T. E. Beechem, C. Saltonstall, A. A. Allerman, A. M. Armstrong, B. A. Klein, A. Bansal, H. R. Seyf, D. Talreja, A. Pogrebnyakov, E. Heller, V. Gopalan, A. S. Henry, J. M. Redwing, B. Foley, and S. Choi, "Interdependence of electronic and thermal transport in $Al_xGa_{1-x}N$ channel HEMTs," IEEE Electron Device Lett. **41**, 461–464 (2020).
[57]A. Karim, Y. Song, D. C. Shoemaker, D.-W. Jeon, J.-H. Park, J. K. Mun, H. K. Lee, and S. Choi, "Thermal analysis of an α-Ga_2O_3 MOSFET using micro-Raman spectroscopy," Appl. Phys. Lett. **123**, 192104 (2023).
[58]Y. Song, A. Bhattacharyya, A. Karim, D. Shoemaker, H.-L. Huang, S. Roy, C. McGray, J. H. Leach, J. Hwang, S. Krishnamoorthy, and S. Choi, "Ultra-wide band gap Ga_2O_3-on-SiC MOSFETs," ACS Appl. Mater. Interfaces **15**, 7137–7147 (2023).
[59]G. Pavlidis, D. Mele, T. Cheng, F. Medjdoub, and S. Graham, "The thermal effects of substrate removal on GaN HEMTs using Raman thermometry," in *15th IEEE Intersociety Conference on Thermal and Thermomechanical Phenomena in Electronic Systems (ITherm)* (IEEE, Las Vegas, NV, 2016), pp. 1255–1260.
[60]J. S. Lundh, D. Shoemaker, A. G. Birdwell, J. D. Weil, L. M. De La Cruz, P. B. Shah, K. G. Crawford, T. G. Ivanov, H. Y. Wong, and S. Choi, "Thermal performance of diamond field-effect transistors," Appl. Phys. Lett. **119**, 143502 (2021).
[61]J. Dallas, G. Pavlidis, B. Chatterjee, J. S. Lundh, M. Ji, J. Kim, T. Kao, T. Detchprohm, R. D. Dupuis, S. Shen, S. Graham, and S. Choi, "Thermal characterization of gallium nitride p-i-n diodes," Appl. Phys. Lett. **112**, 073503 (2018).
[62]J. S. Lundh, T. Zhang, Y. Zhang, Z. Xia, M. Wetherington, Y. Lei, E. Kahn, S. Rajan, M. Terrones, and S. Choi, "2D materials for universal thermal imaging of micro- and nanodevices: An application to gallium oxide electronics," ACS Appl. Electron. Mater. **2**, 2945–2953 (2020).
[63]R. Aubry, J.-C. Jacquet, J. Weaver, O. Durand, P. Dobson, G. Mills, M.-A. Di Forte-Poisson, S. Cassette, and S.-L. Delage, "SThM temperature mapping and nonlinear thermal resistance evolution with bias on AlGaN/GaN HEMT devices," IEEE Trans. Electron Devices **54**, 385–390 (2007).
[64]F. Gucmann, J. W. Pomeroy, and M. Kuball, "Scanning thermal microscopy for accurate nanoscale device thermography," Nano Today **39**, 101206 (2021).
[65]G. Pavlidis, M. S. Jamil, D. Myren, S. Keebaugh, J. Chang, M. Doerflein, S. Afroz, R. S. Howell, and A. Centrone, "Thermal engineering increases current density in AlGaN/GaN superlattice devices," Appl. Phys. Lett. **125**, 012103 (2024).
[66]G. S. Shekhawat, S. Ramachandran, H. Jiryaei Sharahi, S. Sarkar, K. Hujsak, Y. Li, K. Hagglund, S. Kim, G. Aden, A. Chand, and V. P. Dravid, "Micromachined chip scale thermal sensor for thermal imaging," ACS Nano **12**, 1760–1767 (2018).
[67]M. P. West, G. Pavlidis, R. H. Montgomery, F. F. Athena, M. S. Jamil, A. Centrone, S. Graham, and E. M. Vogel, "Thermal environment impact on HfO_x RRAM operation: A nanoscale thermometry and modeling study," J. Appl. Phys. **133**, 185101 (2023).
[68]A. El Sachat, F. Alzina, C. M. Sotomayor Torres, and E. Chavez-Angel, "Heat transport control and thermal characterization of low-dimensional materials: A review," Nanomaterials **11**, 175 (2021).
[69]M. R. Rosenberger, J. P. Jones, E. R. Heller, S. Graham, and W. P. King, "Nanometer-scale strain measurements in AlGaN/GaN high-electron mobility transistors during pulsed operation," IEEE Trans. Electron Devices **63**, 2742–2748 (2016).
[70]J. M. Goodwill, G. Ramer, D. Li, B. D. Hoskins, G. Pavlidis, J. J. McClelland, A. Centrone, J. A. Bain, and M. Skowronski, "Spontaneous current constriction in threshold switching devices," Nat. Commun. **10**, 1628 (2019).
[71]A. R. Zanatta, "Revisiting the optical bandgap of semiconductors and the proposal of a unified methodology to its determination," Sci. Rep. **9**, 11225 (2019).
[72]D. C. Shoemaker, A. Karim, D. Kendig, H. Kim, and S. Choi, "Deep-ultraviolet thermoreflectance thermal imaging of GaN high electron mobility transistors," in *21st IEEE Intersociety Conference on Thermal and Thermomechanical Phenomena in Electronic Systems (iTherm)* (IEEE, San Diego, CA, 2022), pp. 1–5.
[73]D. Kendig, K. Yazawa, and A. Shakouri, "Hyperspectral thermoreflectance imaging for power devices," in *33rd Thermal Measurement, Modeling & Management Symposium (SEMI-THERM)* (IEEE, San Jose, CA, 2017), pp. 204–207.
[74]G. Brocero, D. Kendig, A. Shakouri, Y. Guhel, P. Eudeline, J.-P. Sipma, and B. Boudart, "Innovative submicron thermal characterization method for AlGaN/GaN power HEMTs with hyperspectral thermoreflectance imaging," in *IEEE Compound Semiconductor Integrated Circuit Symposium (CSICS)* (IEEE, Miami, FL, 2017), pp. 1–4.
[75]H. Zhang, S.-B. Wen, and A. Bhaskar, "Two-wavelength thermoreflectance in steady-state thermal imaging," Appl. Phys. Lett. **114**, 151902 (2019).
[76]B. Bista, P. Golani, F. Liu, T. Truttmann, G. Pavlidis, A. Centrone, B. Jalan, and S. Koester, "Evaluating the thermal performance of perovskite $SrSnO_3$ field effect transistors," in *22nd IEEE Intersociety Conference on Thermal and Thermomechanical Phenomena in Electronic Systems (ITherm)* (IEEE, Orlando, FL, 2023), pp. 1–5.
[77]M. J. Tadjer, T. J. Anderson, J. C. Gallagher, P. E. Raad, P. Komarov, A. D. Koehler, K. D. Hobart, and F. J. Kub, "Thermal performance improvement of GaN-on-diamond high electron mobility transistors," in *76th Device Research Conference (DRC)* (IEEE, Santa Barbara, CA, 2018), pp. 1–2.
[78]M. J. Tadjer, T. J. Anderson, M. G. Ancona, P. E. Raad, P. Komarov, T. Bai, J. C. Gallagher, A. D. Koehler, M. S. Goorsky, D. A. Francis, K. D. Hobart, and F. J. Kub, "GaN-on-diamond HEMT technology with $T_{avg} = 176\,^{\circ}C$ at $P_{DC,max} = 56$ W/mm measured by transient thermoreflectance imaging," IEEE Electron Device Lett. **40**, 881–884 (2019).

[79]B. L. Hancock, M. Nazari, J. Anderson, E. Piner, F. Faili, S. Oh, D. Francis, D. Twitchen, S. Graham, and M. W. Holtz, "Ultraviolet and visible micro-Raman and micro-photoluminescence spectroscopy investigations of stress on a 75-mm GaN-on-diamond wafer," Phys. Status Solidi C **14**, 1600247 (2017).
[80]D.-M. Jeon, D.-P. Han, J.-I. Shim, and D.-S. Shin, "Temperature measurements of metal-free GaN using a thermoreflectance-based approach depending on excitation wavelength," Jpn. J. Appl. Phys., Part 1 **64**, 012002 (2025).
[81]G. Pavlidis, D. Kendig, L. Yates, and S. Graham, "Improving the transient thermal characterization of GaN HEMTs," in *17th IEEE Intersociety Conference on Thermal and Thermomechanical Phenomena in Electronic Systems (ITherm)* (IEEE, San Diego, CA, 2018), pp. 208–213.
[82]G. Pavlidis, D. Kendig, E. R. Heller, and S. Graham, "Transient thermal characterization of AlGaN/GaN HEMTs under pulsed biasing," IEEE Trans. Electron Devices **65**, 1753–1758 (2018).
[83]J. S. Lundh, G. Pavlidis, K. Sasaki, A. Centrone, J. A. Spencer, H. N. Masten, M. Currie, A. G. Jacobs, K. Konishi, A. Kuramata, K. D. Hobart, T. J. Anderson, and M. J. Tadjer, "Assessment of channel temperature in β-$(Al_xGa_{1-x})_2O_3/Ga_2O_3$ heterostructure field-effect transistors using visible wavelength thermoreflectance thermal imaging," Appl. Phys. Lett. **124**, 054103 (2024).
[84]C.-H. Ho, C.-Y. Tseng, and L.-C. Tien, "Thermoreflectance characterization of β-Ga_2O_3 thin-film nanostrips," Opt. Express **18**, 16360 (2010).
[85]G. Tessier, G. Jerosolimski, S. Holé, D. Fournier, and C. Filloy, "Measuring and predicting the thermoreflectance sensitivity as a function of wavelength on encapsulated materials," Rev. Sci. Instrum. **74**, 495–499 (2003).
[86]J.-H. Chen, "Simple thin-film fiber optic temperature sensor based on Fabry-Perot interference," Opt. Eng. **49**, 044402 (2010).
[87]G. Pavlidis, "Assessing the performance and reliability of GaN based electronics via optical and electrical methods," Ph.D. dissertation (Georgia Institute of Technology, 2018).
[88]Y. Zhang, M. Liu, D. Jena, and G. Khalsa, "Tight-binding band structure of β- and α-phase Ga_2O_3 and Al_2O_3," J. Appl. Phys. **131**, 175702 (2022).
[89]C. Remple, J. Huso, and M. D. McCluskey, "Photoluminescence and Raman mapping of β-Ga_2O_3," AIP Adv. **11**, 105006 (2021).
[90]L. Binet and D. Gourier, "Origin of the blue luminescence of β-Ga_2O_3," J. Phys. Chem. Solids **59**, 1241–1249 (1998).
[91]L. Binet and D. Gourier, "Optical evidence of intrinsic quantum wells in the transparent conducting oxide β-Ga_2O_3," Appl. Phys. Lett. **77**, 1138–1140 (2000).
[92]F. Shi and H. Qiao, "Preparations, properties and applications of gallium oxide nanomaterials – A review," Nano Select **3**, 348–373 (2022).
[93]G. Pavlidis, M. Jamil, and B. Bista, "(*Invited*) Sub-bandgap thermoreflectance imaging of ultra-wide bandgap semiconductors," in *ECS Meeting Abstracts* (The Electrochemical Society, Inc., 2023), Vol. MA2023-01, p. 1822.
[94]H. Amano, R. Collazo, C. D. Santi, S. Einfeldt, M. Funato, J. Glaab, S. Hagedorn, A. Hirano, H. Hirayama, R. Ishii, Y. Kashima, Y. Kawakami, R. Kirste, M. Kneissl, R. Martin, F. Mehnke, M. Meneghini, A. Ougazzaden, P. J. Parbrook, S. Rajan, P. Reddy, F. Römer, J. Ruschel, B. Sarkar, F. Scholz, L. J. Schowalter, P. Shields, Z. Sitar, L. Sulmoni, T. Wang, T. Wernicke, M. Weyers, B. Witzigmann, Y.-R. Wu, T. Wunderer, and Y. Zhang, "The 2020 UV emitter roadmap," J. Phys. D: Appl. Phys. **53**, 503001 (2020).
[95]A. N. Wilson, K. A. Gupta, B. H. Koduru, A. Kumar, A. Jha, and L. R. Cenkeramaddi, "Recent advances in thermal imaging and its applications using machine learning: A review," IEEE Sens. J. **23**, 3395–3407 (2023).